Chaotic convection in a ferrofluid

D. Laroze[*,a,b], P. G. Siddheshwar[c], H. Pleiner[a]

[a]*Max Planck Institute for Polymer Research, D 55021 Mainz, Germany*
[b]*Instituto de Alta Investigación, Universidad de Tarapacá, Casilla 7D, Arica, Chile*
[c]*Department of Mathematics, Bangalore University, Central College Campus, Bangalore-560001, India*

Abstract

We report theoretical and numerical results on thermally driven convection of a magnetic suspension. The magnetic properties can be modeled as those of electrically non-conducting superparamagnets. We perform a truncated Galerkin expansion finding that the system can be described by a generalized Lorenz model. We characterize the dynamical system using different criteria such as Fourier power spectrum, bifurcation diagrams, and Lyapunov exponents. We find that the system exhibits multiple transitions between regular and chaotic behaviors in the parameter space. Transient chaotic behavior in time can be found slightly below their linear instability threshold of the stationary state.

Key words: Thermal convection, magnetic fluid, chaos.
PACS: 47.50.Gj, 47.55.pb, 47.65.Cb

1. Introduction

Chaotic behavior in thermal convection started with the work of Lorenz in the sixties [1]. The author found chaos in the simplest Rayleigh-Benard convection using a prototype model to forecast the weather. The experimental observation of the chaotic behavior in this system was made by Libchaber and coworkers [2]. Other works in the chaotic convection are in simple fluids [4, 5], in binary fluids [3, 6, 7], in viscoelastic fluids [8–11], in porous media [12–14], in magnetohydrodynamics [15], in magnetic fluids [16] or in dielectrics [17], just to mention a few examples.

Ferrofluids are colloidal suspensions of magnetic nanoparticles dispersed in a carrier liquid. Typically, the particles' diameter is of a few tenths of nanometers leading to gravitationally stable systems. Ferrofluids are superparamagnetic showing a strong response to external magnetic fields [18, 19]. Convection in ferrofluids for different situations has been reported both theoretically [20–45] and experimentally [46–57].

The purpose of the present paper is to analyze the chaotic convective behavior of an electrically nonconducting ferrofluid, in contrast to magnetohydrodynamic systems, where chaotic motion is accompanied by appropriate electric currents. Using a truncated Galerkin expansion, similar to the Lorenz assumption [1], we derive a set of three nonlinear differential equations for the amplitudes of flow, temperature and magnetic potential. We characterize the dynamical behavior of the system through the calculation of Lyapunov exponents, bifurcation diagrams, and Fourier power spectra. Here we report the computation of complete phase diagrams for this generalized Lorenz system that include all physically stable phases, both periodic and chaotic. Generally, this is difficult to obtain, because computationally intensive calculations are needed, particularly for models set up as a system of continuous ordinary differential equations. Recent work describing such methods and difficulties can be found in Ref. [58].

---

[*]Corresponding author at Max Planck Institute for Polymer Research, D 55021 Mainz, Germany. Tel: +49 (0)6131 379165; fax: +49 (0)6131 379340.
Email address: laroze@mpip-mainz.mpg.de (D. Laroze)

The paper is organized as follows: In Section 2, the basic hydrodynamic equations for magnetic fluid convection are presented. In Section 3 the generalized Lorenz equations are derived. In Section 4 the stability analysis of the stationary solutions is calculated. In Section 5 and 6 the numerical simulations are performed and the results are explained. Finally, a summary is given in Section 7.

2. Basic equations

We consider a layer of thickness d, parallel to the xy-plane, with very large horizontal extension, of a ferrofluid subject to a vertical temperature gradient and gravitational field $\mathbf{g} = -g\hat{\mathbf{z}}$. The magnetic fluid properties are modeled as those of an electrically nonconducting superparamagnet. An external vertical magnetic field $\mathbf{H} = H_0\hat{\mathbf{z}}$ is assumed to be present. The static temperature difference across the layer is imposed by fixing the temperatures at the layer boundaries, $T(z = 0) = T_0 + \triangle T$ and $T(z = d) = T_0$. Within the Boussinesq approximation, the dimensionless equations for the perturbations from the quiescent, heat conducting state, can be written as [45]

$$\nabla \cdot \mathbf{v} = \mathbf{0}, \tag{1}$$

$$P^{-1}d_t\mathbf{v} = -\nabla p_{eff} + \nabla^2\mathbf{v} + Ra\mathbf{\Sigma}(\theta, \phi), \tag{2}$$

$$d_t\theta = \nabla^2\theta + v_z, \tag{3}$$

$$(\partial_{zz} + M_3(\partial_{xx} + \partial_{yy}))\phi - \partial_z\theta = 0, \tag{4}$$

$$\nabla^2\phi_{ext} = 0, \tag{5}$$

where $\{\mathbf{v}, \theta, \phi\}$ are the dimensionless perturbations of the velocity, the temperature, and the magnetic potential, respectively. Here $d_t f = \partial_t f + \mathbf{v} \cdot \nabla f$ is the material derivative, p_{eff} is the effective pressure which contains the static hydrodynamic pressure and the gradient term of the magnetic force, and $\mathbf{\Sigma} = \Pi_1(\theta, \phi)\hat{\mathbf{z}} + M_1(\nabla\theta)(\partial_z\phi)$ with $\Pi_1 = (1 + M_1)\theta - M_1\partial_z\phi$.

We have kept four dimensionless numbers in (1)-(5): The Rayleigh number, $Ra = \alpha_T g\beta d^4/\kappa\nu$, accounting for buoyancy effects, the Prandtl number, $P = \nu/\kappa$, relating viscous and thermal diffusion time scales, $M_1 = \beta\chi_T^2 H_0^2/(\rho_0 g\alpha_T(1+\chi))$ describing the strength of the magnetic force relative

to buoyancy, and $M_3 = (1 + \chi)/(1 + \chi + \chi_H H_0^2)$, a measure for the deviation of the magnetization curve from the linear behavior $M_0 = \chi H_0$. In these dimensionless numbers different physical quantities appear such as ρ_0 the reference mass density, c_H the specific heat capacity at constant volume and magnetic field, χ_T the pyromagnetic coefficient, κ the thermal diffusivity, χ_H the longitudinal magnetic susceptibility, α_T the thermal expansion coefficients, α_H the magnetic expansion coefficients, ν the static viscosity, and $\beta = \triangle T/d$ the applied temperature gradient.

The Rayleigh number Ra is the main control parameter and can be varied by several orders of magnitude, relevant values in the present case are $Ra \sim 10^2 - 10^3$. Typical value for P in ferrofluids are $P \sim 10^0 - 10^3$ with $P \sim 10$ for aqueous systems. The magnetic numbers are field dependent with $M_1 \sim 10^{-4} - 10^2$ and $M_3 \gtrsim 1$ for typical magnetic field strengths [27]. Note that M_1 is directly proportional to H_0^2, while M_3 is only a weak function of the external magnetic field. Other magnetic numbers have been suppressed, since their values are of the order 10^{-5} in ferrofluids, with negligible effects on the balance equations [27].

3. Generalized Lorenz equations

In this section we derive a set of ordinary differential equations using a truncated Galerkin method in the same spirit as Lorenz [1]. For the sake of simplicity, the analysis is limited to two-dimensional flows. In particular, we assume a two-dimensional pattern, which is laterally in the x-direction infinite and periodic with wave number k, describing parallel convection rolls along the y-axis. In this case, we express the velocity field in terms of the stream function, ψ, defined by $\mathbf{v} = \{-\partial_z\psi, 0, \partial_x\psi\}$. Therefore, the set of equations can be written as

$$
\begin{aligned}
P^{-1}d_t\nabla_+^2\psi &= Ra([1 + M_1]\partial_x\theta - M_1\partial_{xz}\phi) \\
&\quad + RaM_1([\partial_x\theta][\partial_{zz}\phi] - [\partial_z\theta][\partial_{xz}\phi]) \\
&\quad + \nabla_+^4\psi, \tag{6} \\
d_t\theta &= \partial_x\psi + \nabla_+^2\theta, \tag{7} \\
0 &= (\partial_{zz} + M_3\partial_{xx})\phi - \partial_z\theta, \tag{8}
\end{aligned}
$$

2

where $d_t f = \partial_t f + [\partial_x \psi][\partial_z f] - [\partial_z \psi][\partial_x f]$, $\nabla_+^2 f = \partial_{xx} f + \partial_{zz} f$ and $\nabla_+^4 f = \partial_{xxxx} f + 2\partial_{xxzz} f + \partial_{zzzz} f$. We impose idealized boundary conditions at $z = (0, 1)$ for the temperature, the scalar magnetic potential and the stream function, respectively

$$\theta = \psi = \partial_z^2 \psi = \partial_z \phi = 0. \qquad (9)$$

For the numerical simulations in the lateral direction we will restrict ourselves to the fundamental mode, neglecting higher harmonics in the x-direction. This assumption can be made since we consider a large container. In the z-direction across the layer a multimode description will be used where necessary. Higher harmonics describe deviations of the variables from the linear regime. According to the boundary conditions we can expand the functions in the following way [1]

$$k\,\psi(t, z, x) = -a_1(t) \sin(\pi z) \sin(kx), \qquad (10)$$

$$\theta(t, z, x) = a_2(t) \sin(\pi z) \cos(kx) + a_3(t) \sin(2\pi z), \qquad (11)$$

$$\phi(t, z, x) = a_4(t) \cos(\pi z) \cos(kx) + a_5(t) \cos(2\pi z). \qquad (12)$$

Note that similar to the Lorenz model we consider the effect of second harmonics only in the temperature (and consequently in the scalar magnetic potential). The second harmonic of the stream function has been neglected under the assumption of small convective motions [1]. This term could be important for the study of large-scale convection.

Substituting these trial functions into Eqs. (6)-(8), multiplying the equations by the corresponding orthogonal eigenfunctions, and integrating in space over the wavelength of a convection cell, $\int_{-\frac{\pi}{k}}^{\frac{\pi}{k}} \int_0^1 dx\, dz$, yields a set of ordinary differential equations for the time evolution of the amplitudes

$$\frac{1}{P} \dot{a}_1(t) = -q^2 a_1(t) - q^4 r a_2(t)[1 - M_{13} a_3(t)], \qquad (13)$$

$$\dot{a}_2(t) = -q^2 a_2(t) - a_1(t) - \pi a_1(t) a_3(t), \qquad (14)$$

$$\dot{a}_3(t) = -4\pi^2 a_3(t) + \frac{\pi}{2} a_1(t) a_2(t), \qquad (15)$$

where $q^2 = \pi^2 + k^2$, $r = Ra/Ra_s$, and $M_{13} = \pi k^2 M_1 M_3/(\pi^2 + k^2[1 + M_1]M_3)$. Here Ra_s is the stationary Rayleigh number obtained from linear stability analysis [20]

$$Ra_s = \frac{q^6(k^2 M_3 + \pi^2)}{k^2 \left(k^2[1 + M_1]M_3 + \pi^2\right)}.$$

We remark that the equation for the scalar magnetic potential is independent of time and the magnetic amplitudes are slaved and determined by $a_4(t) = -\pi a_2(t)/(k^2 M_3 + \pi^2)$ and $a_5(t) = -a_3(t)/(2\pi)$. Note that this set of three differential equations can be viewed as a generalized Lorenz system for ferrofluid convection. The magnetic effects in Eq. (13) appear in the nonlinear term proportional to $a_2 a_3$. Note that similar systems were presented in Ref. [16] and in Ref. [17] for magneto- and electro-convection, respectively. In the following section Eqs. (13) - (15) are analyzed in detail.

Apart from the two dimensional roll pattern considered here, the system could exhibit three dimensional patterns like square or hexagonal ones. To compare their stability range with the roll patterns requires a complete three dimensional analysis, which is well beyond the scope of the present work.

4. Stability analysis

For the analysis of our generalized Lorenz system it is convenient to use an equivalent normalization defining a new time scale $\tau = q^2 t$ and new variables $A(\tau) = \pi a_1(\tau)/(q^2 \sqrt{2})$, $B(\tau) = -\pi r a_2(\tau)/\sqrt{2}$ and $C(\tau) = -\pi r a_3(\tau)$. Hence, Eqs. (13) - (15) read as

$$A'(\tau) = P(B(\tau) - A(\tau)) + Q_{13}B(\tau)C(\tau), \quad (16)$$

$$B'(\tau) = rA(\tau) - B(\tau) - A(\tau)C(\tau), \qquad (17)$$

$$C'(\tau) = A(\tau)B(\tau) - \frac{4\pi^2}{q^2} C(\tau), \qquad (18)$$

where $f' = df/d\tau$ and $Q_{13} = PM_{13}/(\pi r)$. Note that when $M_1 \to 0$ or $M_3 \to 0$ ($Q_{1,3} \to 0$) and $q^2 \to q_{RB}^2 = 3\pi^2/2$, the Lorenz system is exactly recovered. We remark that the generalized system still has the reflection symmetry $\{A, B, C\} \to \{-A, -B, C\}$ of the original Lorenz

3

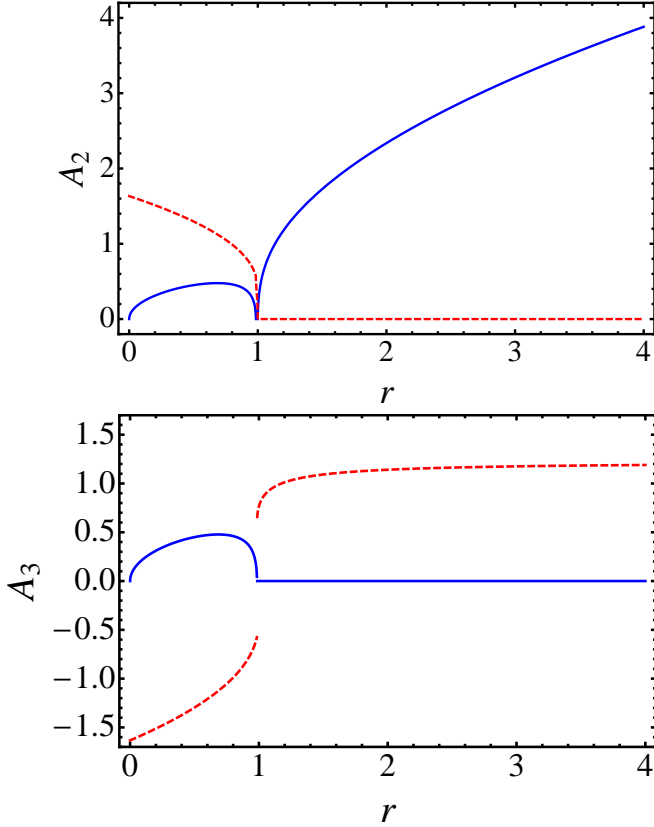Figure 1: The flow amplitudes A_2 and A_3 of the stationary solutions as a function of the reduced Rayleigh number r. Solid (blue) lines show the real parts, while dashed (red) ones depict imaginary parts. Only A_2 is real for $r > 1$ and describes the stationary, homogeneous convection state. The fixed parameters are $k = \pi/\sqrt{2}$, $P = 10$, $M_1 = 10$, and $M_3 = 1.1$.

system [1], which implies that if $\{A, B\}$ are solutions so are $\{-A, -B\}$. The latter degeneracy will not be shown explicitly in the following. We will now analyze the stability of the fixed points and perform full numerical simulations.

The system of Eqs. (16)-(18) has the general form $\mathbf{Y}' = \mathbf{F}(\mathbf{Y})$ with $\mathbf{Y} = \{A, B, C\}$. There are five stationary solutions (two of which are degenerate), which are calculated from $\mathbf{Y}' = \mathbf{0}$. The first one is the trivial, motionless solution $\mathbf{Y}_1 = \{0, 0, 0\}$, which exists for any value of the control parameter r. Generally, there are other solutions

$$A_{2,3} = \frac{\sqrt{P\eta\Psi_\pm}\left(\pm\sqrt{\Phi} + P + rQ_{13}\right)}{2\sqrt{2}PQ_{13}}, \quad (19)$$
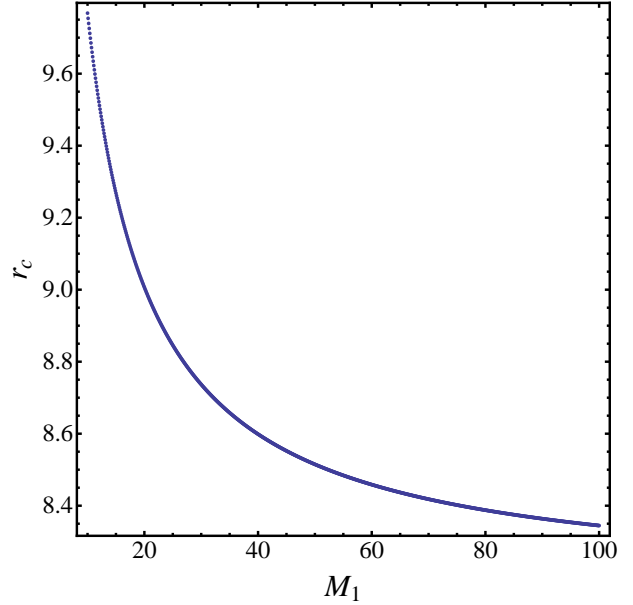

Figure 2: Critical reduced Rayleigh number r_c, where the stationary convection state becomes linearly unstable, as a function of $M_1 \sim H_0^2$. The fixed parameters are $k = \pi/\sqrt{2}$, $P = 10$, $M_3 = 1.1$.

$$B_{2,3} = \frac{\sqrt{P\eta\Psi_\pm}}{\sqrt{2}Q_{13}}, \quad (20)$$

$$C_{2,3} = \frac{rQ_{13} - P \pm \sqrt{\Phi}}{2Q_{13}}, \quad (21)$$

where $\eta = 4\pi^2/q^2$, $\Psi_\pm = \pm\sqrt{\Phi} - P - Q_{13}(-2+r)$, and $\Phi = P^2 + 2PQ_{13}(-2+r) + Q_{13}^2r^2$. These solutions describe stationary convection, only when they are real. Indeed, in the case $r > 1$ there is $\Phi > 0$ and $\Psi_\pm \gtrless 0$ meaning that one solution $\mathbf{Y}_2 = \{A_2, B_2, C_2\}$ is real and describes a stationary convective state, while $\mathbf{Y}_3 = \{A_3, B_3, C_3\}$ does not (since A_3 and B_3 are imaginary). For $r < 1$ both solutions are complex, since $\Psi_\pm < 0$, and do not describe a physical realizable state. In Fig. 1 the typical behavior of A_2 and A_3 is shown as a function of r. The former state converges to the trivial one at $r = 1$, equivalently to the Lorenz system [1], while the latter is non-zero and imaginary, due to a non-zero Q_{13}. We note that for $r > 1$ there are two real solutions, A_2 and the trivial one, $A_1 = 0$, whose stability we will consider next.

To analyze the stability of each homogeneous solution $\mathbf{Y}_H$ let us suppose that $\mathbf{Y}(\tau) = \mathbf{Y}_H + \delta\mathbf{Y}(\tau)$ where $\delta\mathbf{Y}(\tau)$ is a fluctuation such that
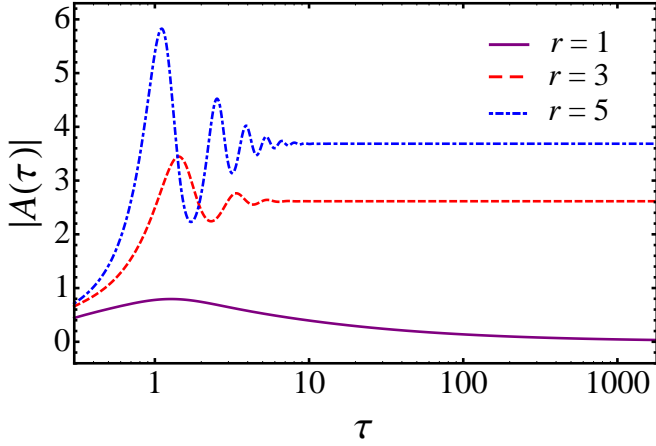
Figure 3: (Color Online) Stream function amplitude, $A(\tau)$, as a function of time τ for three different values of r in the stationary regime for $M_1 = 1$, $M_3 = 1.1$, $k = \pi/\sqrt{2}$ and $P = 10$. The purple (continuous), red (dashed), and blue (dashed-dotted) curves are for $r = 1, 3, 5$, respectively.

$|\delta\mathbf{Y}| \ll 1$. The linearized equation around $\mathbf{Y}_H$ is $\delta\mathbf{Y}' = \bar{\mathbf{J}} \cdot \delta\mathbf{Y}$ where $\bar{\mathbf{J}}$ is the Jacobian matrix

$$\bar{\mathbf{J}} = \begin{pmatrix} -P & P + C_H Q_{13} & B_H Q_{13} \\ r - C_H & -1 & -A_H \\ B_H & A_H & -\eta \end{pmatrix}. \quad (22)$$

The associated eigenvalue problem of $\bar{\mathbf{J}}$ produces the secular equation (with $\delta\mathbf{Y}' = \zeta\delta\mathbf{Y}$)

$$\zeta^3 + p_2\zeta^2 + p_1\zeta + p_0 = 0, \quad (23)$$

where

$$p_2 = 1 + P + \eta \quad (24)$$

$$\begin{aligned} p_1 &= \eta + P(1 - r + \eta) + A_H^2 - B_H^2 Q_{13} \\ &+ C_H^2 Q_{13} + C_H(P - rQ_{13}), \end{aligned} \quad (25)$$

$$\begin{aligned} p_0 &= P(\eta(1 - r) + A_H^2) - B_H^2 Q_{13} \\ &+ C_H(P\eta - r\eta Q_{13} + 2A_H B_H Q_{13}) \\ &+ A_H B_H(P - rQ_{13}) + \eta C_H^2 Q_{13}. \end{aligned} \quad (26)$$

The stability of the stationary solution depends on the sign of ζ and the transition from stability to instability occurs when the real part of one or more of the eigenvalues passes through a zero from negative to positive.

In the case of $\mathbf{Y}_1$ the eigenvalues are $\zeta_1 = -\eta$ and $2\zeta_{2,3} = -1 - P \pm \sqrt{(-1 + P)^2 + 4rP}$. The
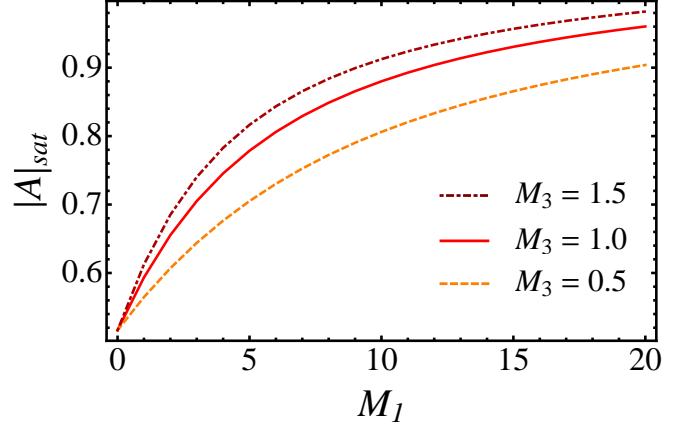

Figure 4: Saturation value of the stream function amplitude A, $|A|_{sat} = |A(\tau \to \infty)|$, as a function of M_1 for three different values of M_3 for $r = 1.1$, $k = \pi/\sqrt{2}$ and $P = 10$. The orange (dashed), red (continuous), and dark-red (dashed-dotted) curves are for $M_3 = 0.5, 1.01, 5$, respectively.

first and third ones are always negative, while the second one changes sign from negative to positive at $r = 1$. Since the marginal instability condition is $\zeta = 0$, $\mathbf{Y}_1$ becomes linearly unstable at $r_c = 1$, independent of the magnetic field. In the case of $\mathbf{Y}_2$ and $\mathbf{Y}_3$ the expressions are much more complicated, which implies that analytical predictions are not tractable, but one can calculate numerically the critical thresholds. Fig. 2 shows the critical reduced Rayleigh number, where the stationary convection state $\mathbf{Y}_2$ becomes linearly unstable. This secondary instability threshold decreases with the magnetic field ($M_1 \sim H_0^2$), hence the magnetic field has a destabilizing effect. This result is in agreement with the linear stability analysis obtained by Finlayson [20]. How the loss of stability of the stationary state is related to the onset of chaos, will be shown below.

5. Numerical simulations

In order to study numerically the dynamical behavior of our system we have integrated Eqs. (16) - (18) via a classical explicit fourth order Runge-Kutta integration scheme with a fixed time step $\triangle t = 0.01$ guaranteeing a precision of 10^{-8} for the amplitudes. For each set of parameters we let the numerical solution evolve for at least 10^6 time steps in order to exclude transient phenom-
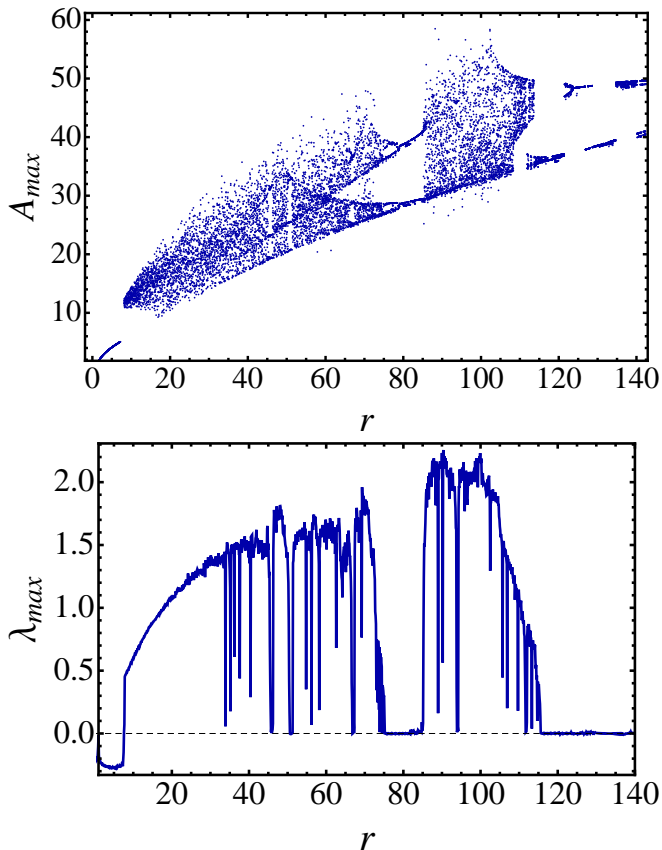
5

Figure 5: The upper frame shows the bifurcation diagram of A as a function of r. In the lower one the maximum Lyapunov exponent, λ_{max} is plotted as a function of r. The fixed parameters are $k = \pi/\sqrt{2}$, $P = 10$, $M_3 = 1.1$ and $M_1 = 20$.
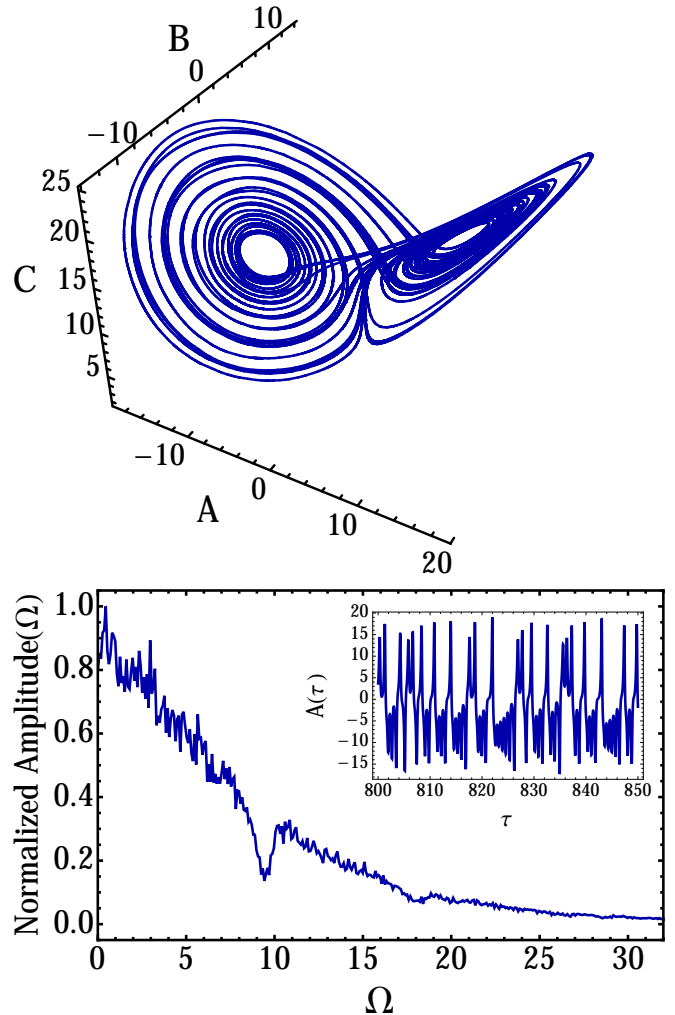

Figure 6: The top frame shows the 3D phase portrait of $\{A, B, C\}$ in the chaotic regime at $r = 15$. The bottom frame shows the corresponding Fourier power spectrum of A and, as inset, the appropriate time series. The fixed parameters are the same as in Fig. (5)

ena. In the plots, where the time dependence of a quantity is shown, we adjust the time window to the relevant dynamical properties under consideration. This system is a generalization of the Lorenz system, hence we expect that the system can exhibit complex behavior.

In the stationary convection state, after some transient oscillations (Fig. 3), the stream function amplitude, A, takes its constant saturation value $|A_{sat}| = |A(t \to \infty)|$. The amplitudes of the transient oscillations as well as the saturation amplitudes increase with the reduced Rayleigh number r (For $r = 1$ the final amplitude is zero, of course). The saturation amplitudes are discussed as a function of the magnetic parameters in Fig. 4. Just above the threshold ($r = 1.1$) they increase strongly with the magnetic field (M_1) and only slightly with the magnetization nonlinearity M_3.

In order to investigate how the system changes its dynamical behavior as a function of the control parameter, in particular to find out what happens close and above the (secondary) instability of the stationary convection regime, we determine the bifurcation diagram and calculate the largest Lyapunov exponent (LE). The bifurcation diagram (upper frame of Fig. 5) is obtained by taking repeatedly the maximum value of the stream function amplitude A_{max} in a given time interval; this is done for a large range of different values of the control parameter r. If there is always the same A_{max}, then the system is periodic, while for finite continuous distribution of different A_{max} values,
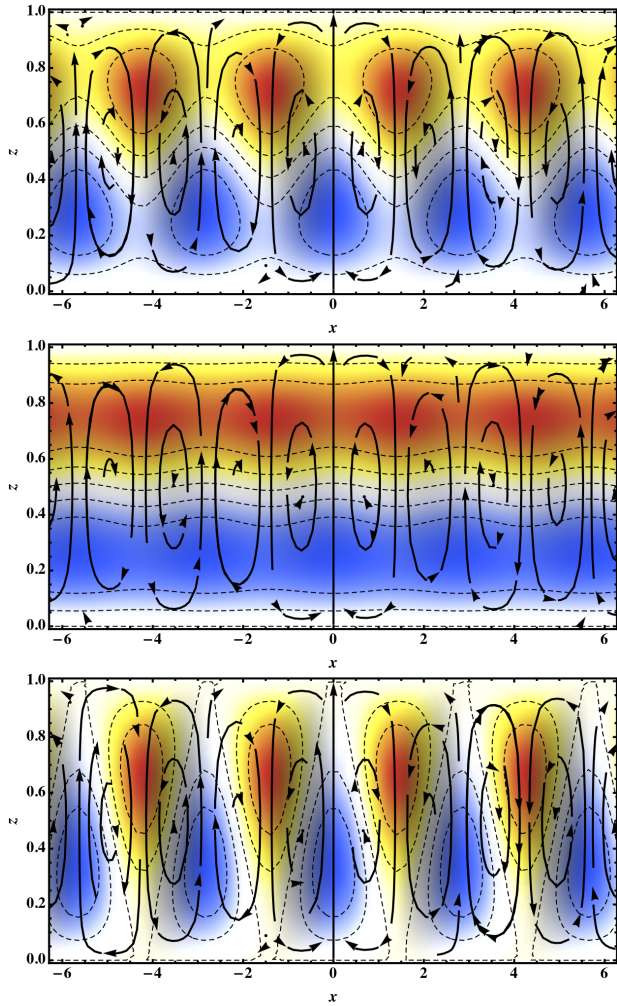
Figure 7: Color coded temperature profiles and streamlines as a function of the spatial coordinates x and z at three different times in the chaotic regime at $r = 15$. Red / upper half layer (blue / lower half layer) mean hotter (colder) regions. The fixed parameters are $k = \pi/\sqrt{2}$, $P = 10$, $M_3 = 1.1$, and $M_1 = 20$. The full time evolution is shown in a movie [63].

Figure 8: Magnetic field lines appropriate to the temperature profiles and streamlines shown in Fig. 7.

the behavior is either quasi-periodic or chaotic. To discriminate between the two latter possibilities, LEs λ_i defined by

$$\lambda_i = \lim_{\tau \to \infty} \frac{1}{\tau} \ln\left(\frac{\|\delta Y_i(\tau)\|}{\|\delta Y_i(0)\|} \right),$$

are considered. LEs are numbers that quantify whether the distance between two initially close trajectories δY_i of a vector field $\mathbf{Y}$, subject to an evolution equation $dY_i/d\tau = F^i(\mathbf{Y}, \tau)$, vanishes (LE negative) or diverges exponentially (LE positive). The latter is the hallmark of a chaotic behavior. Our basically 3-dimensional phase space
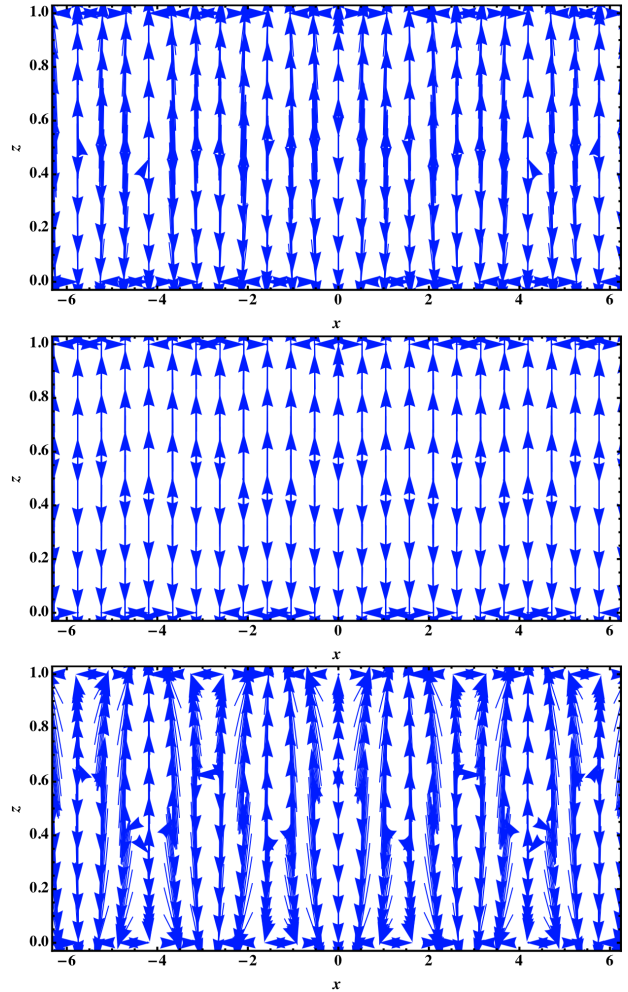
carries 3 LEs [58–62], which can be ordered in descending form, with the largest Lyapunov exponent denoted by λ_{max}. The error E in the evaluation of the LEs has been checked by using $Err = \sigma(\lambda_M) / \max(\lambda_M)$, where $\sigma(\lambda_M)$ is the standard deviation of λ_{max}. In all cases studied here E is of the order of 1%, which is sufficiently small for the purpose of the present analysis.

6. Results

In Fig.5 the transition from the stationary to the chaotic behavior at $r \approx 7.8$ is clearly visible, since A_{max} becomes continuous and λ_{max} positive above this secondary instability. The chaotic regime, however, is interrupted by (two smaller) regimes (at roughly $r = 45$ and 50) and a larger regime (between $r \approx 75$ and $r \approx 85$), where the
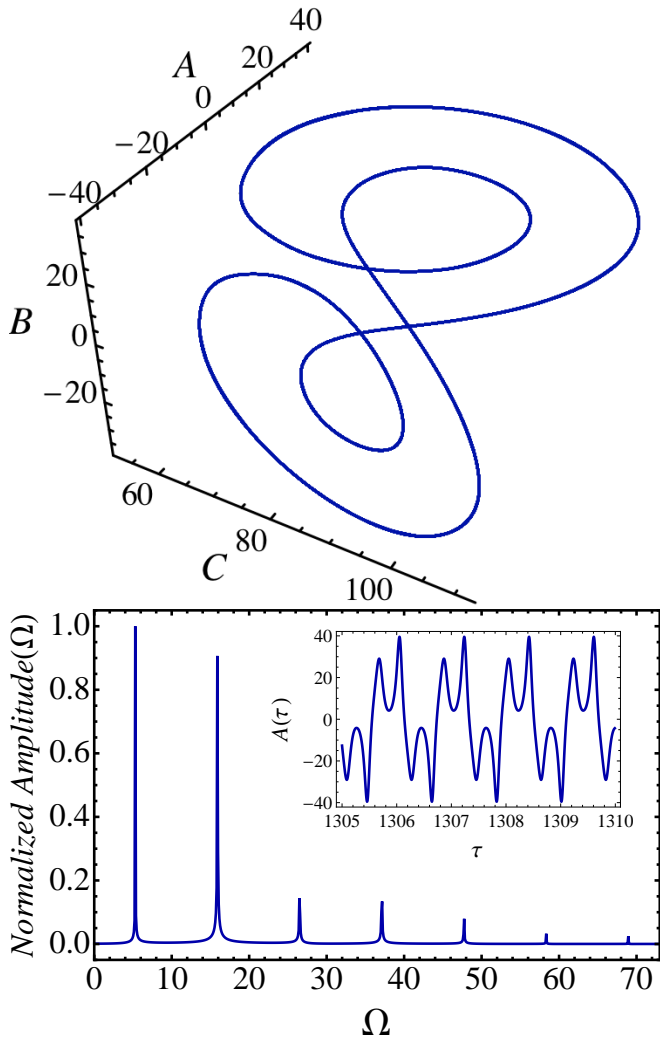
Figure 9: The top frame shows 3D phase portrait of $\{A, B, C\}$ in the periodic window at $r = 82$. The bottom frame shows the corresponding Fourier power spectrum of A and, as inset, the time series of A. The fixed parameters are $k = \pi/\sqrt{2}$, $P = 10$, $M_3 = 1.1$, and $M_1 = 20$.

Figure 10: (Color online) Phase diagram displaying the largest Lyapunov exponent color coded as a function of the field amplitudes M_1 and M_3 for $k = \pi/\sqrt{2}$, $P = 10$ and $r = 7.8$. The resolution is $\triangle M_1 = 0.1$ and $\triangle M_3 = 0.05$.

system is regular (e.g. $\lambda_{max} = 0$). For very high values of the control parameter, $r \gtrsim 116$, chaos is suppressed. However, there is the possibility that chaotic states reappear for even higher r values, beyond those we have considered here, in a way similar to the Lorenz model [64–66]. In the following, we will discuss as examples the chaotic dynamic behavior at $r = 15$ and the periodic one in the large regular window ($r = 82$). Finally, we investigate transient chaotic regimes that are pronounced for intermediate magnetic fields.

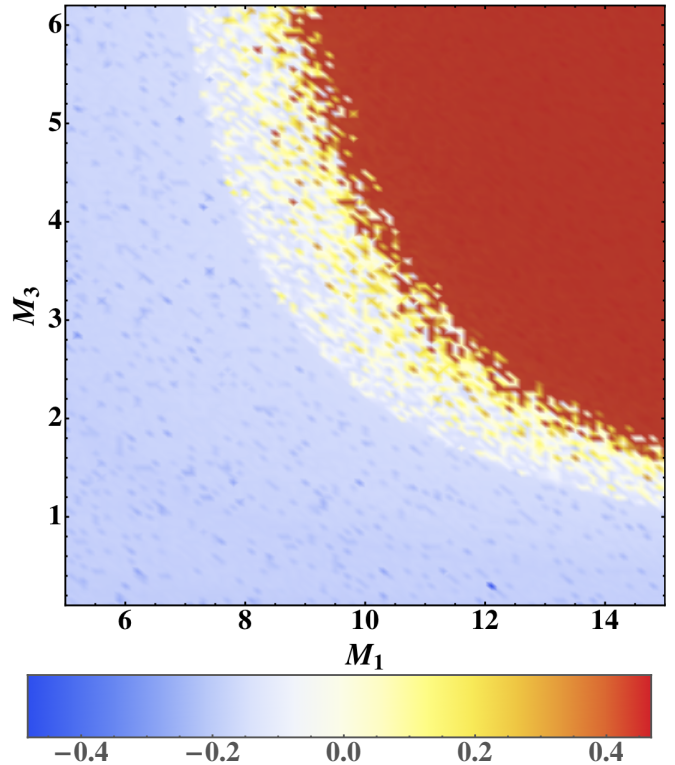Figs. 6-8 show the system in the chaotic regime. In the top frame of Fig. 6 the 3D phase portrait reveals a strange attractor of similar shape as the Lorenz attractor. In the bottom frame the Fourier power spectrum of the stream function amplitude A and its corresponding time series (inset) is shown. The time dependence is aperiodic and, as a consequence, the Fourier power spectrum is continuous, characteristic for chaotic behavior. To compute the Fourier spectrum in the chaotic regime we have done the calculations for 50 different random initial conditions. In Fig. 7 the temperature profile and the streamlines in the chaotic regime are depicted as a function of the spatial coordinates x and z for three different times. A movie, included as complementary material, demonstrates the chaotic nature of the temperature profile as a function of space and time [63]. In Fig. 8 the appropriate magnetic field profiles are shown.

In Fig. 9 we show one example of behavior in the regular window at $r = 82$. The top frame shows the 3D phase portrait and in the bottom
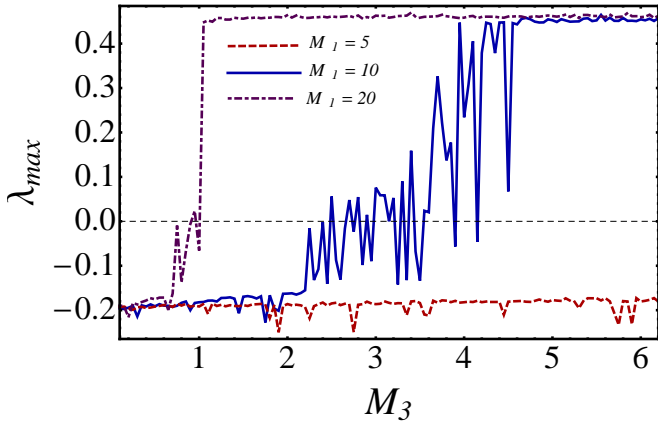
Figure 11: Largest Lyapunov exponent, λ_{max}, as a function of M_3 for $M_1 = 5$ (red, dotted curve), $M_1 = 10$ (blue, continuous curve), and $M_1 = 20$ (purple, dash-dotted curve), for $k = \pi/\sqrt{2}$, $P = 10$, and $r = 7.8$.
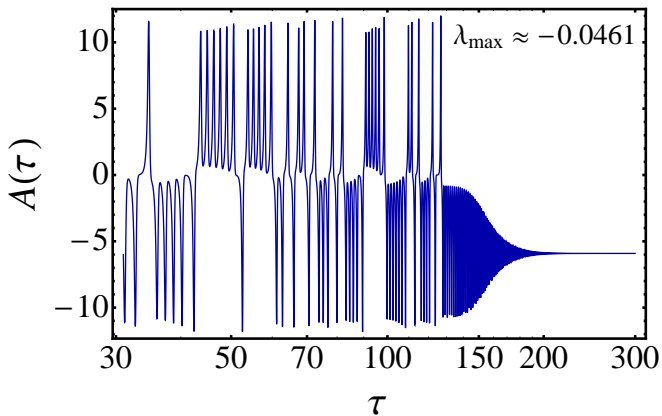

Figure 12: Time series of A in a chaotic transient regime for $k = \pi/\sqrt{2}$, $P = 10$, $r = 7.8$, $M_1 = 10$ and $M_3 = 4.15$.

one the Fourier power spectrum of A and its corresponding time series (inset) is presented. We observe that the trajectory is a closed orbit and there are only discrete peaks in the Fourier spectrum, which is expected for a regular (periodic or quasi-periodic) motion.

Above, we have discussed the dynamic behavior as a function of the applied temperature gradient. We now switch to the dependence on the external magnetic field. For somewhat smaller external fields and larger magnetic field nonlinearity, the transition between the stationary regime and the chaotic one is more complicated. Fig. 10 shows a color-coded λ_{max} phase diagram as a function of both magnetic numbers, M_1 and M_3 for a

fixed value of r. For small values of M_1 and M_3 λ_{max} is negative and the system regular, while for larger values of these parameters there is chaos. However, the transition region is not sharp, but diffuse, presenting multiple transitions between chaotic to regular motion. In order to understand this transition three cuts of the phase diagram at different values of M_1 are plotted in Fig. 11. For low M_1 there is no transition, while for large M_1 the transition at increasing M_3 is almost direct from stationary to chaotic. In the intermediate case, $M_1 = 10$ there is a series of stationary-chaos transitions in broad range of M_3 values, before for larger M_3 the chaotic state prevails. For one of these intermediate stationary states at $M_3 = 4.15$, where $\lambda_{max} = -0.0461$, $A(\tau)$ is shown in Fig. 12. There is a transient chaotic behavior preceding the stationary state. Such transitions take place at a time scale that is by a factor of 20 smaller than our maximum integration time. Changing slightly M_3, a true chaotic state with positive λ_{max} is found.

For the material parameters ($M_1 = 20$, $M_3 = 1.1$) chosen in the phase diagram Fig. 5 a higher resolution picture (Fig. 13) shows a very tiny regime ($r \approx 7.7 - 7.8$) with a few transient chaotic solutions, before for $r \gtrsim 7.8$ the chaotic regime is reached. Note, that this transition occurs well before the linear stability of the stationary state breaks down at $r_c = 9.1$, cf. Fig.2. This phenomenon that a strange attractor appears at a reduced Rayleigh number smaller than the critical threshold r_c from the linear stability analysis, also happens in the Lorenz system [64].

Finally, we have looked at the Prandtl number dependence. Fig. 14 shows a color-coded λ_{max} phase diagram as a function of the magnetic number M_1 and the Prandtl number P. Here, the chaotic region occurs in a compact pattern of a rather characteristic shape. For small $P \lesssim 4$ there is no chaos for any M_1. Similarly, chaos is suppressed for high P values, where the relevant P decreases with decreasing M_1.
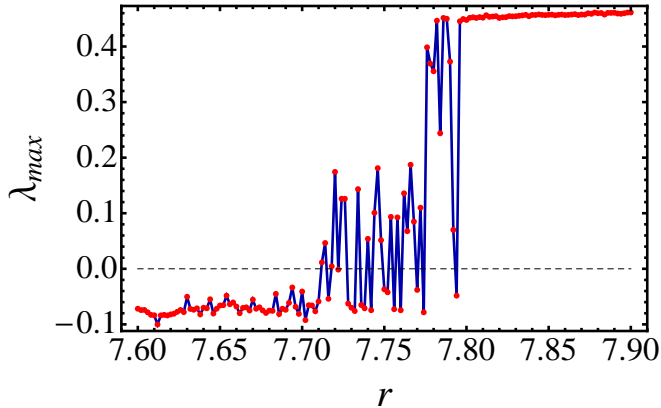
Figure 13: Higher resolution version of the phase diagram Fig. 5 near the stationary to chaotic transition ($k = \pi/\sqrt{2}$, $P = 10$, $r = 7.8$, $M_1 = 10$ and $M_3 = 4.15$).

7. Summary

We have studied the nonlinear convection of a ferrofluid in the two-dimensional spatial case. In particular we have derived a set of three ordinary nonlinear differential equations, which describe as a minimal model the complex dynamic behavior in the presence of an external magnetic field. Without a magnetic field the classical Lorenz model is recovered. We have identified parameter regions, where stationary states or those with chaotic or regular dynamics occur, using the Lyapunov exponent method, bifurcation diagrams, and phase portraits. We have performed intensive numerical simulation to get time series and power spectra of the stream function amplitude as well as spatial temperature profiles in the chaotic regime. We have found that the system has multiple transitions between regular and chaotic behavior in parameter space. Close to the transition from the stationary to a chaotic state, which occurs slightly below the linear stability boundary, the stationary states show transient chaotic behavior in time. Finally, we remark that our generalized Lorenz system has certain similarities with the one found for dielectric liquids subject to AC electric fields [17]; the complete comparison between both systems will be presented in future works.
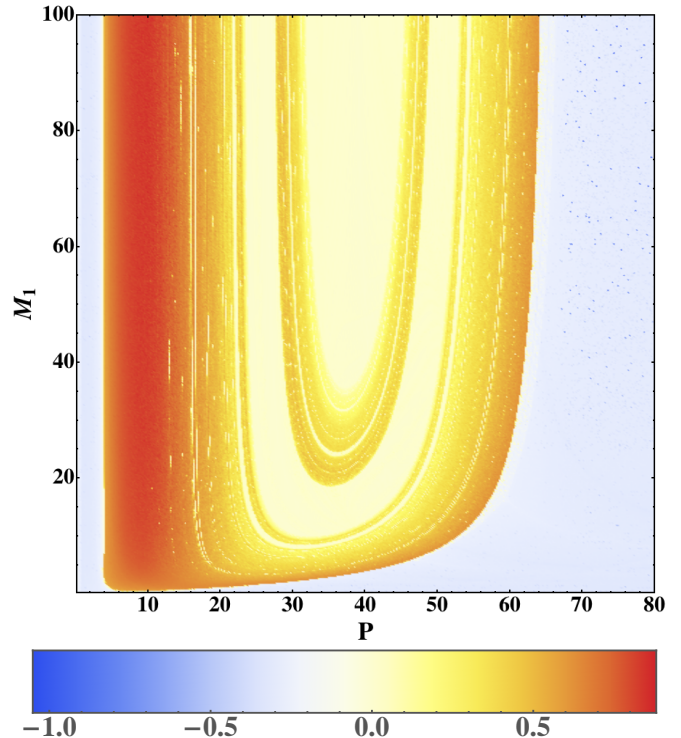

Figure 14: (Color online) Phase diagram displaying the largest Lyapunov exponent λ_{max} color coded as a function of the field amplitude M_1 and the Prandtl number P for $k = 3$, $r = 15$ and $M_3 = 1.1$. The resolution is $\triangle P = 0.2$ and $\triangle M_1 = 0.2$.

8. Acknowledgments

References

[1] E.N. Lorenz, J. Atmos. Sc. **20**, 130 (1963).

[2] J. Stavans, F. Heslot, and A. Libchaber, Phys. Rev. Lett. **55**, 596 (1985)

[3] J.K. Bhattacharjee *Convection and Chaos in Fluids*, (World Scientific Publishing, Singapur, 1987); and references therein.

[4] A. P. Vincent and D. A. Yuen, Phys. Rev. A **38**, 328 (1988).

[5] A. Jayaraman, J. D. Scheel, H. S. Greenside, and P. F. Fischer Phys. Rev. E **74**, 016209 (2006)

[6] R. W. Walden, Paul Kolodner, A. Passner, and C. M. Surko, Phys. Rev. Lett. **55**, 496(1985).

[7] A. E. Deane, E. Knobloch, and J. Toomre, Phys. Rev. A **36**, 2862 (1987).

[8] R.E. Khayat, J. Non-Newtonian Fluid Mech. **53**, 227 (1995).

[9] E. Abu-Ramadan, J. M. Hay, R. E. Khayat, J. Non-Newtonian Fluid Mech. **115**, 79 (2003).

[10] L.J. Sheu, L.M. Tam, J.H. Chen, H.K. Chen, K.T. Lin, Y. Kang, Chaos Solitons Fractals **37**, 113 (2008).

[11] P.G. Siddheshwar, G.N. Sekhar, G. Jayalatha, J. Non-Newtonian Fluid Mech. **165**, 1412 (2010).

[12] P. Vadasz, S. Olek, Int. J. Heat Mass Transfer **41**, 1417 (1998).

[13] L.J. Sheu, Chaos Solitons Fractals **30**, 672 (2006).

[14] J.M. Jawdat, I. Hashim, Int. Comm. Heat Mass Transfer **37**, 629 (2010).

[15] M.N. Mahmud, I. Hashim, International Communications in Heat and Mass Transfer **38**, 481 (2011).

[16] I. Kobori and H. Yamaguchi, J. Magn. Magn. Mater. **122**, 290 (1993).

[17] P.G. Siddheshwar and D. Radhakrishna, Commun. Nonlinear Sci. Numer. Simulat. **17**, 2883 (2012).

[18] S. Odenbach, *Magnetoviscous Effects in Ferrofluids* (Springer Lecture Notes in Physics, Berlin, 2002).

[19] S. Odenbach (ed.), *Colloidal Magnetic Fluids* (Springer Lecture Notes in Physics, Berlin, 2009).

[20] B.A. Finlayson, J. Fluid Mech. **40**, 753 (1970).

[21] K. Gotoh and M. Yamada, J. Phys. Soc. Jpn. **51**, 3042 (1982).

[22] P.J. Blennerhassett, F. Lin and P.J. Stiles, Proc. R. Soc. London A **433**, 165 (1991).

[23] M.D. Gupta and A.S. Gupta, Int. J. Eng. Sci. **17**, 271 (1979).

[24] S. Venkatasubramanian and P.N. Kaloni, Int. J. Eng. Sci. **32**, 237 (1994).

[25] P.N. Kaloni and J.X Lou, J. Magn. Magn. Mater. **284**, 54 (2004).

[26] G.K Auernhammer and H.R. Brand, Eur. Phys. J. **B16**, 157 (2000).

[27] A. Ryskin and H. Pleiner, Phys. Rev. E **69**, 046301 (2004).

[28] D. Laroze, J. Martinez-Mardones, J. Bragard and P. Vargas, Physica A **371**, 46 (2006).

[29] D. Laroze, J. Martinez-Mardones, L.M. Pérez and Y. Rameshwar, Int. J. Bif. Chaos, **19**, 2755 (2009).

[30] Y. Qin and P.N. Kaloni, Eur. J. Mech. B/Fluids **13**, 305 (1994).

[31] P. G. Siddheshwar, J. Magn. Magn. Mater. **149**, 148 (1995).

[32] M.I. Shliomis and M. Souhar, Europhys. Lett. **49**, 55 (2000).

[33] I.S. Shivakumara, N. Rudraiah, and C.E. Nanjundappa, J. Magn. Magn. Mater. **248**, 379 (2002).

[34] P. G. Siddheshwar, Int. J Mod. Phys. B **16** 2629, (2002).

[35] P.N. Kaloni and J.X. Lou, Phys. Rev. E **70**, 026313 (2004).

[36] P.N. Kaloni and J.X. Lou, Phys. Rev. E **71**, 066311 (2005).

[37] S. Odenbach and Th. Volker, J. Magn. Magn. Mater. **289**, 122 (2005).

[38] R. Sekar, G. Vaidyanathan, R. Hemalatha and S. Sendhilnathan, J. Magn. Magn. Mater. **302**, 20 (2006)

[39] Sunil, P. Sharma and A. Mahajan, Heat. Trans. Res. **40**, 351 (2009).

[40] Sunil, P. Chandb, P.K. Bhartia,and A. Mahajan, J. Magn. Magn. Mater. **320**, 316 (2008).

[41] D. Laroze and J. Martinez-Mardones, AIP Conf. Proc. **913**, 9 (2007).

[42] D. Laroze, J. Martinez-Mardones and L.M. Pérez, Int. J. Bif. Chaos **20**, 235 (2010).

[43] D. Laroze, J. Martinez-Mardones and L.M. Pérez, R.G. Rojas, J. Mag. Mag. Mat. **322**, 3576 (2010).

[44] L.M. Pérez, J. Bragard, D. Laroze, J. Martinez-Mardones and, H. Pleiner, J. Mag. Mag. Mat. **323**, 691 (2011).

[45] D. Laroze, L.M. Pérez, J. Bragard, E.G. Cordaro, and J. Martinez-Mardones , Magnetohydrodynamics. **47**, 159 (2011).

[46] D. Braithwaite, E. Beaugnon, and R. Tournier, Nature **354**, 134 (1991).

[47] S. Odenbach, Phys. Fluids **6**, 2535 (1994).

[48] S. Odenbach, D. Schwahn, and K. Stierstadt, Z. Phys. B **96**, 567 (1995).

[49] S. Odenbach, J. Magn. Magn. Mater. **149**, 155 (1995).

[50] H. Yamaguchi, I. Kobori, Y. Uehata, and K. Shimada, J. Magn. Magn. Mater. **201**, 264 (1999).

[51] S. Odenbach, J. Phys.: Condens. Matter **15**, S1497 (2003).

[52] S. Odenbach and Th. Vlker, J. Magn. Magn. Mater. **289**,122 (2005).

[53] H. Engler and S. Odenbach, J. Phys.: Condens. Matter **20**, 204135 (2008).

[54] T. Bednarz, C. Lei, and J.C. Patterson, Int. Comm. Heat Mass Trans. **36**, 97 (2009).

[55] T. Bednarz, J.C. Patterson, C. Lei, and H. Ozoe, Int. Comm. Heat Mass Trans. **36**, 781 (2009).

[56] A. Bozhko and G. Putin, Microgravity Sci. Technol. **21**, 89 (2009).

[57] M. Lajvardi, J. Moghimi-Rad, I. Hadi, A. Gavili, T. Dallali Isfahani, F. Zabihi, and J. Sabbaghzadeh, J. Magn. Magn. Mater. **322**, 3508 (2010).

[58] C. Bonatto and J. A. C. Gallas, Phys. Rev. Lett. **101**, 054101 (2008). G. M. Ramirez-Avila and J. A. C. Gallas, Phys. Lett. A **375**, 143 (2010). J. A. C. Gallas, Int. J. Bif. Chaos **20**, 197 (2010); and references therein.

[59] A. Wolf, J. B. Swift, H. L. Swinney, and J. A. Vastano, Physica D, **16**, 285 (1985).

[60] D. Laroze, J. Bragard, O. J. Suarez, and H. Pleiner, IEEE Trans. Mag. **47**, 3032 (2011).

[61] J. Bragard, H. Pleiner, O. J. Suarez, P. Vargas, J. A.

11

C. Gallas, and D. Laroze, Phys. Rev. E **84**, 037202 (2011)

[62] D. Laroze, D. Becerra-Alonso, J. A. C. Gallas, and H. Pleiner, IEEE Trans. Mag. **48**, 3567 (2012).

[63] A movie of this solution as a complementary material is shown in the website: https://www.dropbox.com/s/g6qp4nb9s3q60r5/animateTemDL.avi

[64] C. Sparrow, *The Lorenz Equations: Bifurcations, Chaos, and Strange Attractors* (Springer, Berlin, 1982).

[65] H.R. Dullin, S. Schmidt,P. H. Richter, S. K. Grossmann, Int. J. Bifur. Chaos **17**, 3013 (2007).

[66] R. Barrio, F. Blesa, S. Serrano, Int. J. Bifur. Chaos **22**, 1230019 (2012).